INTERNATIONAL JOURNAL FOR NUMERICAL METHODS IN FLUIDS
Int. J. Numer. Meth. Fluids 2001; **37**: 601–624 (DOI: 10.1002/fld.193)

Numerical simulation of viscous flows with free surface around realistic hull forms with transom

Tingqiu Li[a,*], Jerzy Matusiak[a] and Reijo Lehtimäki[b]

[a] *Ship Laboratory, Helsinki University of Technology, Helsinki, Finland*
[b] *Laboratory of Aerodynamics, Helsinki University of Technology, Helsinki, Finland*

SUMMARY

This paper describes a method for simulation of viscous flows with a free surface around realistic hull forms with a transom, which has been developed based on a FINFLO RANS solver with a moving mesh. A dry-transom model is proposed and implemented for the treatment of flows off the transom. The bulk RANS flow with the artificial compressibility is solved by a cell-centred finite volume multigrid scheme and the free surface deformed by wave motions is tracked by satisfying the kinematic and dynamic free-surface boundary conditions on the actual location of the surface. The effects of turbulence on flows are evaluated with the Baldwin–Lomax turbulence model without a wall function. A test case is modern container ship model with a transom, the Hamburg Test Case. The calculated results are validated and they agree well with the measured results in terms of the free-surface waves and the total resistance coefficient. Furthermore, the numerical solutions successfully captured many important features of the complicated interaction of the free surface with viscous flows around transom stern ships. In addition, the convergence performance and the grid refinement studies are also investigated. Copyright © 2001 John Wiley & Sons, Ltd.

KEY WORDS: dry-transom model; FINFLO RANS solver; modern hull forms with a transom; moving mesh; viscous free surface flows

1. INTRODUCTION

Realistic motion of ships in turbulent flow is always complex in the presence of the free surface. The prediction of the physical process is a more complicated problem that requires full knowledge of the interaction of the wave structure with the viscous boundary layer. With the advent of powerful computers for numerical calculation, it is possible for application of the advanced computational fluid dynamic (CFD) techniques to resolve the mathematical model, which describes the mechanism of the interaction. Furthermore, the total ship resistance experienced by an advancing ship at a constant forward speed can be evaluated in a numerical

* Correspondence to: Ship Laboratory, Helsinki University of Technology, PO Box 4100 (Otakaari 4), FIN-02015 HUT, Finland.

Received 3 May 2000
Revised 21 February 2001

water tank, and it is one of the main interests of industry. Therefore, it is desirable to develop a reliable and robust method in order to enhance greatly the hull design capabilities.

The early approaches in this area are the finite difference (FD) methods [1,2]. Later works can be found from [3,4]. Recently published papers are given in [5,6]. Tahara and Stern [7] developed a finite-analytic (FA) method. For these approaches, the governing equations with non-conservative form are solved and the location of the free surface is determined in the computational domain up to the viscous sublayer. On the other hand, an interactive approach [8,9] is, respectively, to solve the Reynolds-averaged Navier–Stokes (RANS) equations with the free surface in the near-wall field and the potential flow in the far field by the panel method. This method can save CPU time considerably but the definition of the interface between two domains requires special attention. In particular, the wake behind the stern covers a wide range, which causes the division of the interface between a viscous flow and an ideal flow not to be clear. A current major approach is to apply a finite volume (FV) method that satisfies the conservation of mass and momentum over the whole computational domain. It is also basic in four current popular CFD codes: PHOENICS, FLUENT, FLOW3D and STAR-CD. Using a FV method, Miyata [10] developed a computer code for ship flow problems. The calculated results seem to reveal some interesting features for the HSVA tanker model at a low ship speed. This is a very full hull form but different from fast container vessels. A moving mesh, that is, the so-called interface-fitting method, has been widely implemented, where the boundary conditions at the interface are given explicitly. Two test cases for simple ship models, the Wigley hull and the Series 60 (S60) ship, have been achieved.

Nevertheless, a comparison of the wave pattern obtained by most methods that represent the major advances with the experimental data is not satisfactory even for the S60 ship model. Some reason may be found in grid resolution for the wave propagation [11]. Hino [12] investigated grid dependency. It is thought that the wave fields away from the hull are significantly influenced by grid spacing. Alessandrini [13] obtained a significant improvement in convergence rate past the S60 ship model with the O-O topology grid based on the fully coupled algorithm. The O-O or O-C topology grid seems to be promising for resolution of ship flow problems [14], although the O-H grid is the most popular grid topology. For transom stern ships, the type of grid suitable is necessitated, especially in the transom domain due to the singularity of the transom corner for fluid flow [15]. Furthermore, it is a more difficult case in view of the physical sensitivity in the prediction of viscous free surface flows off a transom [16]. One approach is to introduce the technique of domain decomposition according to the region of interest, such as at the transom stern, and to use the multiblock strategy [17,18]. The application of unstructured grids is also interesting [19]. In particular, problems like overturning at a bulbous bow as well as unsteady bubbling or boiling behind a transom stern [20] may be encountered and have to be avoided during the simulation. For improvement of the stability of the free-surface computations, the former could be filtered with the local extremum diminishing (LED) principle [17], and the latter can be approximated by the use of the dry-transom model of enforcing the water to detach from the base of the transom junction [21].

Using a moving mesh creates moderate distortion of the free surface. For more complex configurations of interest, such as breaking waves or topology changes, the moving grid system becomes somewhat unrefined. An alternative is to use the interface-capturing methods, e.g. the

volume of fluid (VOF) method [22,23], the marker and cell (MAC) methods [1,2] and the level-set method [24], where the boundary conditions at the interface are approximately satisfied on a predetermined fixed grid, which extends to the air region but is not fitted to the free surface. Takafumi [25] suggested that a sufficient number of grid points are required for construction of fine grid spacing when using the density-function method similar to the VOF method. Otherwise, the accuracy is inferior to that with a moving mesh. This may be improved with the adaptive grid [26] and the Chimera grid blocks [27].

The principal objective of the present study is to develop a computational method that can simulate complex viscous free-surface flows around realistic hull forma with a transom. The free surface is tracked by introducing a moving body-fitted grid system according to wave motions. A dry-transom model for the treatment of flows behind a transom is proposed. A container ship, the Hamburg Test Case (HTC), provide by the Hamburg Ship Model Basin (HSVA), Germany, and recommended by ITTC, is selected as the test case. Only steady state flow is studied in the present case. The FINFLO RANS solver [28], the treatment of the free surface and the dry-transom model are described in Section 2, and then the results and discussion are given for the HTC model in Section 3. Some concluding remarks are made in Section 4.

2. NUMERICAL METHODS

2.1. Mathematical models

For resolution of ship wave problems in the Cartesian reference co-ordinate system Oxyz (see Figure 1), where the origin O is fixed at the intersection of the bow with the still free surface, x is positive in the aft direction, y is positive towards the starboard and the z-direction is positive upwards, the RANS equations can be written in the following compact form:

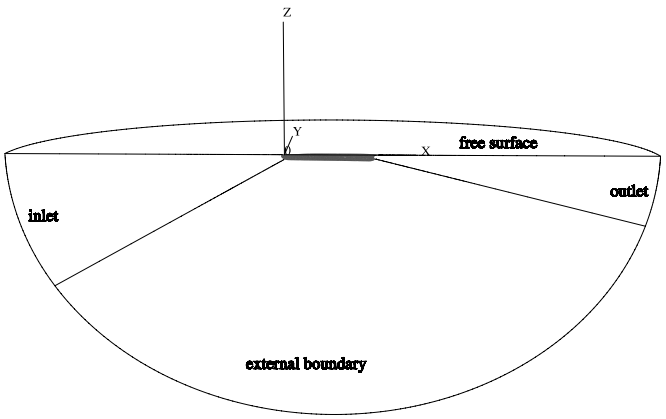

Figure 1. A reference co-ordinate system around the HTC model.

$$\frac{\partial U}{\partial t}+\frac{\partial (F-F_v)}{\partial x}+\frac{\partial (G-G_v)}{\partial y}+\frac{\partial (H-H_v)}{\partial_z}=0 \tag{1}$$

where $U=(\rho, \rho u, \rho v, \rho w)^T$. ρ is the density of the fluid, and u, v, and w are the velocity components in the x-, y- and z-directions respectively. These are chosen as the dependent variables and the independent variables are the co-ordinates x, y, z and time t. If the turbulent kinematic energy k and the gravitational force g are included in the total pressure p, then inviscid fluxes F, G and H in Equation (1) are

$$F=\begin{pmatrix} \rho u \\ \rho u^2+\psi \\ \rho vu \\ \rho wu \end{pmatrix}, \qquad G=\begin{pmatrix} \rho v \\ \rho uv \\ \rho v^2+\psi \\ \rho wv \end{pmatrix}, \qquad H=\begin{pmatrix} \rho w \\ \rho uw \\ \rho vw \\ \rho w^2+\psi \end{pmatrix} \tag{2}$$

with

$$\psi=p+\frac{2}{3}k+\rho gz \tag{3}$$

In the present method, the so-called piezometric pressure ψ is solved instead of p. The viscous fluxes F_v, G_v and H_v are

$$F_v=\begin{pmatrix} 0 \\ \tau_{xx} \\ \tau_{xy} \\ \tau_{xz} \end{pmatrix}, \qquad G_v=\begin{pmatrix} 0 \\ \tau_{xy} \\ \tau_{yy} \\ \tau_{yz} \end{pmatrix}, \qquad H_v=\begin{pmatrix} 0 \\ \tau_{xz} \\ \tau_{yz} \\ \tau_{zz} \end{pmatrix} \tag{4}$$

In expression (4), the viscous stress tensors, τ_{ij} $(i, j=1, 2, 3)$, are defined as

$$\tau_{ij}=\mu\left(\frac{\partial u_i}{\partial x_j}+\frac{\partial u_j}{\partial x_i}-\frac{2}{3}(\nabla\cdot\mathbf{V})\delta_{ij}\right)-\rho\overline{u_i'u_j'} \tag{5}$$

Based on Boussinesq's approximation, the Reynolds stresses, $\rho\overline{u_i'u_j'}$, are written in the form of

$$\rho\overline{u_i'u_j'}=\mu_t\left(\frac{\partial u_i}{\partial x_j}+\frac{\partial u_j}{\partial x_i}-\frac{2}{3}(\nabla\cdot\mathbf{V})\delta_{ij}\right)-\frac{2}{3}\rho k\delta_{ij} \tag{6}$$

where $\mathbf{V}=u\vec{i}+v\vec{j}+w\vec{k}$ and $\mu=\rho v$. v is the kinematic viscosity of 1.01×10^{-6} m^2 s^{-1} and δ_{ij} is the Kronecker's symbol. μ_t is the turbulent viscous coefficient and its value is dependent on the turbulence model employed. Equations (5) and (6) are written in tensor notation with the usual summation convention assumed. The last term $-\frac{2}{3}\rho k$ in Equation (6) has been absorbed to the piezometric pressure ψ.

The artificial compressibility [29] is introduced and added to the term of $\partial\rho/\partial\psi$ in order to enforce incompressibility. Hence, the resulting expression for the speed of sound c becomes [30]

$$\frac{1}{c^2} = \frac{1}{c_0^2} + \frac{1}{c_{\text{true}}^2} \tag{7}$$

and c_0 is the artificial compressibility coefficient. It is formulated as

$$c_0 = \zeta_t \sqrt{u^2 + v^2 + w^2} \tag{8}$$

in which ζ_t is a constant between 3 and 10 [31]. Furthermore, the equation of the state of motion for a compressible fluid is given by

$$\psi = c_0^2 \rho \tag{9}$$

2.2. Solution procedures

A cell-centred FV method is used for discretization of the integral form of the conservation Equation (1), which can be derived from the differential form by integrating over a control volume and applying the Gauss theorem. Following the general approaches within the cell-centred FV method, Equation (1) can be expressed as

$$\frac{\partial}{\partial t} \int_V U \, \mathrm{d}V + \int_S \mathbf{F}(U) \cdot \mathrm{d}\mathbf{S} = 0 \tag{10}$$

for an arbitrary fixed region V with a boundary S. Since the computational domain is divided into a set of hexahedrons, the integration for each cell yields

$$V \frac{\partial U}{\partial t} = \sum_{\text{face}} - S\hat{\mathbf{F}} \tag{11}$$

where the sum is taken over the faces of the computational cell, and the inviscid fluxes and viscous fluxes for the face are defined as

$$\hat{\mathbf{F}} = n_x(F - F_v) + n_y(G - G_v) + n_z(H - H_v) \tag{12}$$

where n_x, n_y and n_z are the normal components of the surface outwards in the x-, y- and z-directions respectively. F, F_v, G, G_v, H and H_v are the fluxes defined by Equations (2)–(4).

The inviscid fluxes are evaluated from the method of Roe [32], and the MUSCL-type approach is used for extrapolation of the solution vectors on the left and right states of the cell surface. In addition, the viscous fluxes are solved with a thin-layer approximation that can be activated in any co-ordinate direction and the velocity at the cell surface is obtained as an average from the nodal values. For integration of Equation (11) in time, the DDADI-factorization based on the approximate factorization as well as the splitting of the Jacobian flux terms [33] is employed. Thus, Equation (11) can be written after factorization as follows:

$$\left[I+\frac{\Delta t}{V}\left(\partial_i^- S_{i+1/2}A_i^+ - \partial_i^+ S_{i-1/2}A_i^-\right)\right]$$

$$\times\left[I+\frac{\Delta t}{V}\left(\partial_j^- S_{j+1/2}B_j^+ - \partial_j^+ S_{j-1/2}B_i^-\right)\right]$$

$$\times\left[I+\frac{\Delta t}{V}\left(\partial_k^- S_{k+1/2}C_k^+ - \partial_k^+ S_{k-1/2}C_k^-\right)\right]\times \Delta U=\frac{\Delta t}{V}R \tag{13}$$

This is the implicit stage. Since the sweeps are based on a first-order upwind-difference scheme, Equation (13) forms a tridiagonal matrix and consists of a backward and forward sweep in every co-ordinate direction. It is noted that $\partial^-_{i,j,k}$ and $\partial^+_{i,j,k}$ are first-order spatial difference operations in the i-, j-, and k-directions respectively, Δt is the local time-step dependent of the Courant number, R is the right-hand side of Equation (11), and A, B, and C are the corresponding Jacobian matrices and calculated, such as for $A^{\pm}$, by

$$A^{\pm}=R(\Lambda^{\pm}+kI)R^{-1} \tag{14}$$

where $\Lambda^{\pm}$ are diagonal matrices containing the positive and negative eigenvalues, and k is a factor for the diagonally dominant factorization in that it can ensure the stability of the viscous term in the calculation.

The multigrid method [34] is implemented to improve the convergence properties of the solution variables. The algorithm used a sequence of coarser meshes that are generated independently. Each coarser gird may be constructed by merely connecting every second grid point in each co-ordinate direction. The solution on grid level h_i is driven by the residuals obtained on grid level h_{i-1} (where h_i denotes the grid level and h_1 the finest level). Hence Equation (1) can be rewritten as

$$\frac{\partial U}{\partial t}=R \tag{15}$$

where R is the residual and defined as

$$R=\sum -S\hat{\mathbf{F}} \tag{16}$$

The solution vectors on grid level h_i are first initialized based on those at the fine grid level h_{i-1}, and then the new residual is obtained from the sum of residual of Equation (16) and the forcing function. The solution vectors and the residual on grid level h_{i-1} are transferred to the next coarser grid level h_i; and they are performed as respectively

$$U^i_{h_i}=\sum V_{h_{i-1}}U_{h_{i-1}}/V_{h_i} \tag{17}$$

and

$$R'_{h_i} = \sum R^*_{h_{i-1}} \tag{18}$$

where the sum is taken over the cells which approximately occupy the cell on the coarse grid.

This procedure of evaluation of the solution vectors and the residual is repeated until the coarsest grid level is reached. Finally, the corrections are transferred back to the finer levels with an interpolation operator. A V-cycle of the multigrid method is implemented in this case. A more detailed description is given in [35].

2.3. Turbulence modelling

The introduction of a turbulence model is necessary for the present mathematical model at a very high Reynolds number of 10^6–10^9, such as the sub-grid scale (SGS) model [10], the k–ε or k–ω turbulence models [13], and the Baldwin–Lomax (B–L) turbulence model [36]. Of all these models, the B–L model is common due to its simplicity, in which the boundary layer is removed and the effects of the transition on turbulence are neglected in evaluation of the turbulence viscosity. Furthermore, the current study [13] shows that the wave fields around the S60 hull are not strongly dependent on the turbulent model, whereas the best performance is offered for the total drag coefficient by the k–ε model in comparison with the algebraic model of the B–L as well as the one-equation model for the American combatant ship DDG51 (INSEAN model 2340) [18]. This is, probably, because the model 2340 is more complex than the S60.

In this paper, the B–L model is chosen based on the studies [30,37]. It is a two-layer, isotropic eddy viscosity formulation and performs well for problems that do not exhibit large regions of separated flow. In this model the turbulent viscosity is evaluated by

$$\mu_t = \begin{cases} \mu_{t,\text{inner}} & \text{if } y \le y_{co} \\ \mu_{t,\text{outer}} & \text{otherwise} \end{cases} \tag{19}$$

where y is the normal distance from the wall and y_{co} is the minimum value of y at which the values of μ_t from the inner and outer match. The inner viscosity follows

$$\mu_t = \rho l^2 |\omega| \tag{20}$$

where $|\omega|$ represents the magnitude of the vorticity and is calculated by

$$|\omega| = \left[\left(\frac{\partial v}{\partial x} - \frac{\partial u}{\partial y} \right)^2 + \left(\frac{\partial w}{\partial y} - \frac{\partial v}{\partial z} \right)^2 + \left(\frac{\partial u}{\partial z} - \frac{\partial w}{\partial x} \right)^2 \right]^{1/2} \tag{21}$$

and

$$l = ky(1 - \mathrm{e}^{-y^+/A_0^+}) \tag{22}$$

In the outer layer the viscosity is given by

$$\mu_t = \rho \alpha C_{\mathrm{cp}} F_{\mathrm{wake}} F_{\mathrm{kleb}} \tag{23}$$

where α is the Clauser constant, C_{cp} is the additional constant and F_{wake} is expressed as

$$F_{\mathrm{wake}} = \min(y_{\max} F_{\max}, C_{wk} y_{\max} U_{\mathrm{diff}}^2 / F_{\max}) \tag{24}$$

The quantities $F_{\max}$ and $y_{\max}$ are determined from the function

$$F(y) = y|\omega|(1 - \mathrm{e}^{-y^+/A_0^+}) \tag{25}$$

in which $F_{\max}$ is the maximum value of $F(y)$ that occurs in a profile and $y_{\max}$ is the value of y at which it occurs. In the wake, the exponential term of Equation (25) is set equal to zero. U_{diff} is the difference between the maximum and the minimum resultant velocity. F_{kleb} is defined

$$F_{\mathrm{kleb}} = \left[1 + 5.5\left(\frac{C_{\mathrm{kleb}} y}{y_{\max}}\right)^6\right]^{-1} \tag{26}$$

The corresponding model constants are given in Table I.

Note that y^+ in Equation (22) is the non-dimensional distance from the wall and is defined as

$$y^+ = \frac{\rho y u_\tau}{\mu} \tag{27}$$

where $u_\tau = (\tau_{\mathrm{w}}/\rho)^{1/2}$. τ_{w} is the wall stress and is evaluated by $\tau_{\mathrm{w}} = \mu\, \partial u/\partial y$ without the law of the wall on the wall. In the present case, $y^+ \approx 1.6$.

2.4. Boundary conditions

2.4.1. Free surface boundary conditions. The boundary conditions on the free surface consist of one kinematic and three dynamic conditions. The kinematic condition on the free surface state that the free surface is a material surface and it may be expressed in the form of

Table I. Empirical coefficients in the B–L model

k	α	A_0^+	C_{cp}	C_{kleb}	C_{wk}
0.41	0.0168	26	1.6	0.3	1.0

$$\frac{\partial h}{\partial t} + (u - u_g)\frac{\partial h}{\partial x} + (v - v_g)\frac{\partial h}{\partial y} = \omega \quad \text{on } z = h(x, y, t) \tag{28}$$

where $h(x, y, t)$ is the wave height with respect to the undisturbed free-surface. u_g and v_g are the velocity components of the grid movement, which are often ignored but may reduce the convergence rate to a steady state, although this treatment does not affect the accuracy of the solution [12]. The dynamic conditions represent the continuity of the normal and the tangential components of the stresses on the free surface, which give the pressure and the two components of the velocities (u, v) on the free surface respectively. Another component of the velocity (w) is always from the continuity equation [6]. This is a totally different approach proposed by Alessandrini [13], in which the two tangential dynamic condition along with the kinematic condition give three components of the velocities on the free surface and the free surface location is evaluated according to the normal dynamic condition. In the present case, the effects of the surface tension and the free surface turbulent boundary layer are neglected. This results in the approximate normal stress conditions through setting the pressure acting on the free surface to be equal the atmosphere pressure, which is set as zero. As a result, the piezometric pressure ψ on this surface is expressed by

$$\psi = \rho g h \tag{29}$$

This gives the Dirichlet condition for the pressure on the free surface. The condition for the tangential stress is approximated by the following zero normal gradient extrapolation:

$$\frac{\partial u}{\partial n} = \frac{\partial v}{\partial n} = \frac{\partial w}{\partial n} = 0 \tag{30}$$

where n is the component normal to the free surface. In this case, the components of the velocities on the free surface are supposed to be equal to those adjacent to grid points, whereas this is not to satisfy the local conservation of mass in the cell near the free surface. As pointed out by Miyata [10], nevertheless, these simplifications made at the very thin thickness in this region do not seriously influence the accuracy.

Since the body-fitted co-ordinate system is implemented and fixed to the free surface, Equation (29) is conveniently imposed and it is exactly satisfied. With the partial transformation approach, in which only the independent variables (x, y, t) in the physical domain are transformed into non-orthogonal curvilinear co-ordinates (ξ, η, t) in the computational domain, Equation (28) can be rewritten in the following form:

$$\frac{\partial h}{\partial t} = f \tag{31}$$

where the residual f is expressed as

$$f = w - \left(u^* \frac{\partial h}{\partial \xi} + v^* \frac{\partial h}{\partial \eta}\right) \tag{32}$$

with the contravariant velocities u^* and v^*. They are given respectively

$$u^* = (ub_1^1 + vb_2^1)/J \tag{33}$$

$$v^* = (ub_1^2 + vb_2^2)/J \tag{34}$$

where b_i^j is the contravariant basis of the two-dimensional transformation, which is given by

$$b_p^l = \frac{\partial x^s}{\partial \xi^m}\frac{\partial x^t}{\partial \xi^n} - \frac{\partial x^t}{\partial \xi^m}\frac{\partial x^s}{\partial \xi^n}$$

and the Jacobian J is evaluated by

$$J = \det\left(\frac{\partial x^j}{\partial \xi^j}\right)$$

If the second-order explicit Adams–Bashforth scheme is applied for integration of Equation (31) in time, the updated wave height at the next time step $(n+1)$ is given by

$$h^{n+1} = h^n + \frac{1}{2}\Delta t(3f^n - f^{n-1}) \tag{35}$$

where Δt is the time step, which may be set to be different from that in Equation (13) due to our currently uncoupled approach. The spatial derivative of the free surface elevation in Equation (32), such as for the spatial indices i, j, is evaluated with a third-order upwind-difference scheme of

$$\begin{aligned}\frac{\partial h}{\partial \xi} = {} & \text{sign}(1, u^*)(h_{i-2,j} - 4h_{i-1,j} + 6h_{i,j} - 4h_{i+1,j} + h_{i+2,j})/12 \\ & + (h_{i-2,j} - 8h_{i-1,j} + 8h_{i+1,j} - h_{i+2,j})/12\end{aligned} \tag{36}$$

and a similar expression holds for $\partial h/\partial \eta$. Thus, Equation (35) can be solved once the initial conditions and the boundary conditions at the external cell, including the ghost cells surrounding the fluid domain, are given by

$$h(x, y, t) = 0 \quad \text{at } t = 0 \tag{37}$$

and by the mirror condition respectively.

As shown in Equation (28), the numerical singularity is always met at the intersection of the free surface with the hull surface as the components of the velocity on the hull verify the no-slip conditions. We avoid this problem through setting all variables to the centre of the cell, where the wave height on the hull is obtained with a second-order extrapolation. It is found that the calculation is more stable when the wave height in the area close to the hull surface

is extrapolated from that specified outside this region by the use of the linear least-square fit. This is because there is a very large aspect ratio of the grid within the boundary layer, especially for realistic hull form with a bulbous bow and a transom stern. Furthermore, the vortices are significant in the vicinity of the free surface layer [10] and within the boundary layer [13]. As a result, the extrapolation of the wave height advantages for removing wave oscillations. Note that the filtering for the free surface is necessary during the simulation, because it can retain the minimum user-specified region of the extrapolation. More detail is given in Li [38,39].

2.4.2. The dry-transom model. Once the free surface is updated at each iteration by Equation (35), the grid points along the body surface and on the free surface are redistributed using a linear interpolation [40], which is performed based on the predetermined grid that extends to the air region. It works well before the water touches the transom stern. This is because flows off the transom stern are often accompanied with a very complex phenomenon, such as a bubble flow, which may not explain within the present moving mesh system. Based on the LED principle and the so-called essentially local extremum diminishing (ELED) scheme, Cowles [17] introduced locally the lower-order dissipation to the free surface computations in order to prevent similar problems like spray formation or wave breaking at the bow. This may be more suitable for stabilizing the calculation and avoiding the overturning of the waves [41]. Another approach is to extrapolate linearly the wave height in the domain near the hull surface [6]. Without any additional assumptions, Takafumi [25] studied the high-speed transom ship flows using the modified density function technique but this is rather more common for merchant vessels.

Our experience shows that the free-surface waves in the area off the transom always oscillate due to the strong unsteady motions in this region. To improve the stability, the treatment of the free surface downstream of the transom stern is required, and a possible choice is to use the dry-transom model, in which the water is first enforced to detach from the base of the transom junction, such as at the point A (see Figure 2); and then the wave height at this point is set to be equal to the vertical co-ordinate of the transom profile. In our dry-transom model, it is necessary to search the location of the first wave peak along the transverse wave profiles, such as the point B (see Figure 2). The key procedure is to extrapolate linearly the wave height, which prevents the skewness of the deformed mesh on the free surface. The extrapolation range should be restricted to a finite distance, r_{AB} (see Figure 2). Thus, the wave height h_p at the point p between A and B is determined from

$$\left(\frac{1}{r_p}+\frac{1}{r_{AB}-r_p}\right)h_p=\frac{1}{r_p}h_A+\frac{1}{r_{AB}-r_p}h_B \tag{38}$$

where r_p is the distance of the point p to the hull surface. Furthermore, the local directional derivative of the waves in this region must be less than that at the detached point along the vertical direction of the hull surface. Otherwise, the deformed mesh may result in skewness that induces cells of negative volume occurring. A single block O-O type mesh is employed and the calculated results show that this grid is suitable for the treatment of the transom stern and the bulbous bow.

The overall solution procedure is first to solve the bulk RANS flow and to continue three times at each cycle owing to a fully implicit stage when the initial conditions, such as a uniform flow, and the boundary conditions are given. Finally, the free surface is updated based on the

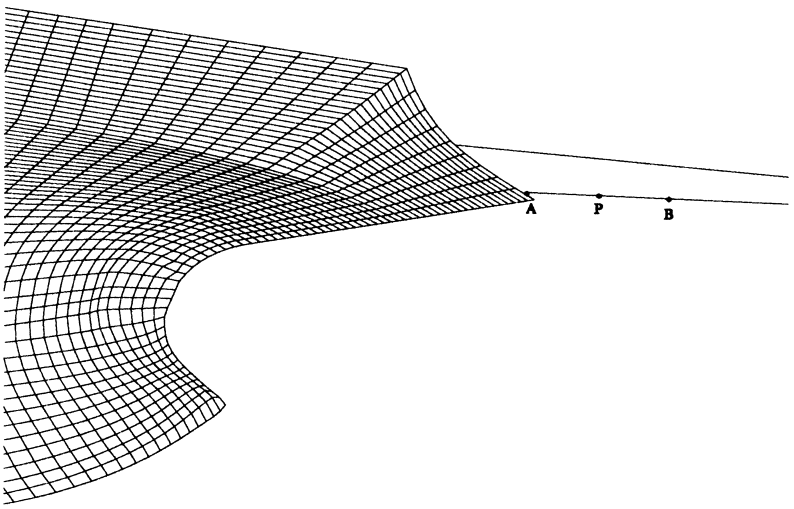

Figure 2. Transom stern treatment, the HTC model. A, detached point; P, extrapolation point; B, wave peak.

extrapolation of the velocity of the bulk RANS flow and the pressure on this surface is adjusted. In addition, the conditions on the other boundaries are renewed. The entire process is repeated until the steady flow state is reached. An example of the deformable mesh at this state is given in Figure 3, which displays the deformable hull surface and the free surface at the bow and the transom respectively. This provides a detailed observation in the region of interest.

2.4.3. Other boundary conditions. No-slip conditions are imposed on the wetted part of the hull surface, that is, all the velocity components on the surface are zero, while the pressure on this surface is obtained by the Neumann (zero gradient) scheme. At the inlet, a uniform flow is given. At the outlet, all variables are extrapolated with the Neumann (zero gradient) approach. On the centreline boundary and the external boundary, the symmetry condition for all variables is implemented. Most of them can be observed in Figure 1.

3. SIMULATION OF TYPICAL MODERN CONTAINER VESSELS

3.1. The HTC model

A typical modern container vessel, the HTC model, is chosen as the test case. It is equipped with a bulbous bow and a transom stern (see Figure 4). The principal dimensions of the ship model, ship length (L) between perpendiculars, breadth (B) and draft (D) at the forward

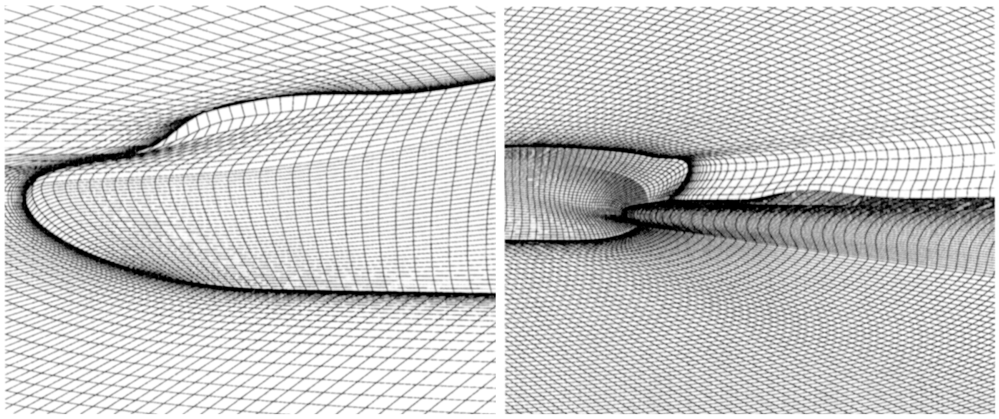

Figure 3. Deformable mesh, the HTC model. Left: at the bow. Right: at the transom.

Figure 4. Side profile, the HTC model.

perpendicular and the aft perpendicular, are $L = 6.404$ m, $B = 1.145$ m, $T_F = 0.383$ m and $T_A = 0.429$ m respectively. The numerical simulation is performed with three grids around the HTC model ($C_B = 0.645$) at a Froude number ($F_n = U/\sqrt{gL}$) of 0.25 and a Reynolds number ($R_n = UL/v$) of 1.255×10^7 based on the reference velocity U, which corresponds to the experimental case at $F_n = 0.249$ and $R_n = 1.232 \times 10^7$ [42]. The finest mesh is $141 \times 129 \times 45$ (818 505 nodes) in the streamwise, the normal and the girth directions respectively. The computational domain (see Figure 1) is $-2.9 \leq x/L \leq 3.8$, $0 \leq y/L \leq 2.8$ and $-2.8 \leq z/L \leq h_{\max}$ (the calculated maximum wave height). One half of the hull is considered for the computations since it is assumed as symmetrical. All the calculations are carried out on a Silicon Graphics Origin2000 Computer provided by the Centre for Scientific Computing (CSC), Finland.

3.2. Mesh structure

A single O-O topology grid around the HTC model is shown in Figure 5, in which the mesh is clustered near the hull surface due to the implementation of the no-slip conditions on the wall without the wall function; the inlet, outlet and external boundaries are located far away from the hull to damp the free-surface waves and to prevent the reflection of the waves at these boundaries. Moreover, to capture the gravitational effects, relative fine mesh is constructed in

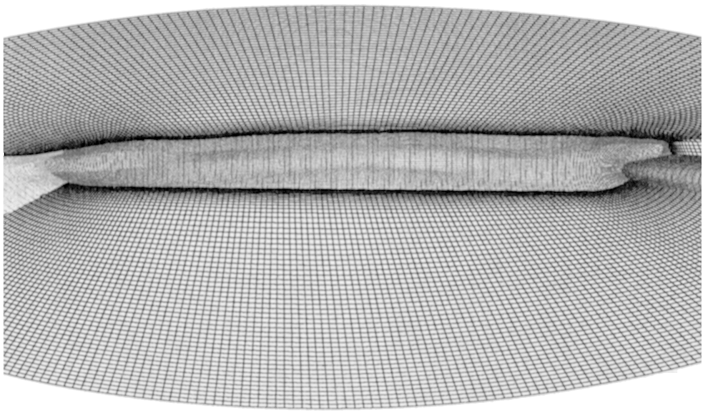

Figure 5. A single O-O topology grid, the HTC model.

the region outside the boundary layer, where the change of the size between the grid points is kept as almost uniform (see Figure 5).

3.3. Convergence history

3.3.1. Momentum and pressure. Figure 6 presents the convergence histories of the L_2 norm of residuals for the momentum (U, V, W) in the x-, y- and z-directions, and the pressure (P) at the coarsest, the medium and the finest mesh respectively. These provide a global measurement of error both in divergence of mass and in conservation of momentum. The residual reduction is the order of below 10^{-5} at the finest mesh (see Figure 6), while the decrease at the coarsest mesh is about 10^{-5}. It appears that the equations for the continuity and the momentum are satisfied to some extent. As a result, the present discrete problem may be achieved with the desired accuracy up to the round-off errors.

3.3.2. Total resistance coefficient, C_T. Figure 7 displays the convergence history of the total resistance coefficient C_T, which is a summation of the tangentially frictional resistance and the total pressure integration, at varying levels respectively. It is non-dimensionalized by $1/2\rho U^2 S$, where S is the reference wetted-surface area. The calculated total resistance coefficient (C_T) at the finest mesh is $C_T = 4.421 \times 10^{-3}$ in the steady state, which is closer to the experimental value of $C_T = 4.222 \times 10^{-3}$ with the relative error of 4.7 per cent, as shown in Figure 7. This is very encouraging in that the comment with regard to convergence and accuracy is mainly from its information. Note that the total CPU time required at the finest mesh is expensive (about 5 days) as compared to that (about 1.8 days and 10 h) for the medium mesh and the coarsest mesh respectively. It is expected that a parallel multiblock approach will be implemented in the near future.

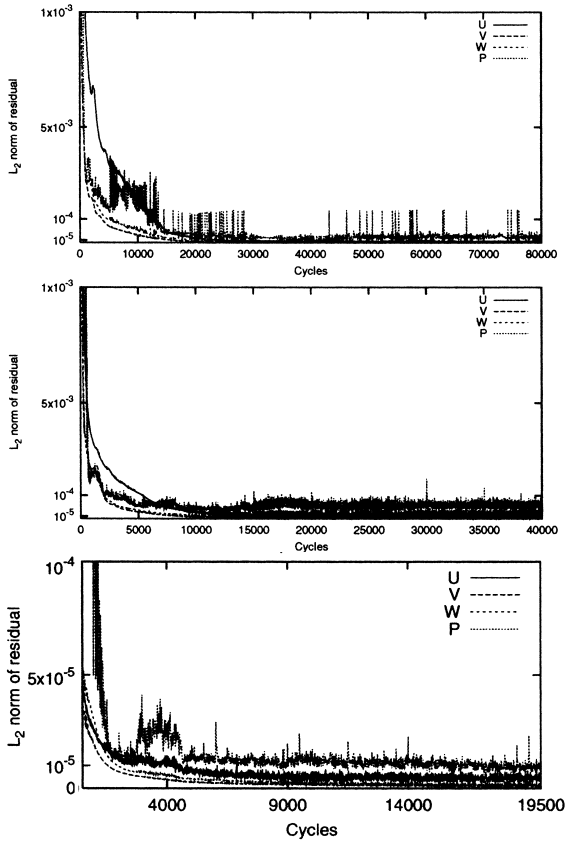

Figure 6. Convergence histories of L_2 norm of residuals for (U, V, W, P), the HTC model ($F_n = 0.25$ and $R_n = 0.255 \times 10^7$). Top: at the coarsest mesh ($36 \times 33 \times 12$). Middle: at the medium mesh ($71 \times 65 \times 23$). Bottom: at the finest mesh ($141 \times 129 \times 45$).

3.4. Grid refinement study

The dependence of the grid size on the free-surface waves and C_T is studied with three grid levels (see Table II). The coarsest mesh (level-3) is $36 \times 33 \times 12$, the medium mesh (level-2) is $71 \times 65 \times 23$ and the finest mesh (level-1) is $141 \times 129 \times 45$ with the refinement ratio of 2 in each co-ordinate direction. Figure 8 shows the surface-wave profiles for these three levels. The profiles are drawn in the region from the bow ($x/L = -0.5$) to the stern ($x/L = 0.5$) and the values of the wave height are made dimensionless with the ship length (L). It is clear that the difference of all the curves is rather small, except for level-3, where the grid points seem to be too small. Furthermore, the wave profiles for level-2 can be comparable with the experimental data, whereas C_T at this level is poor (see Table II). In this case, a minimum spacing of grid in the y-direction is 1.06×10^{-5} and the value of y^+ is 3.2. Thus, one can conclude that the

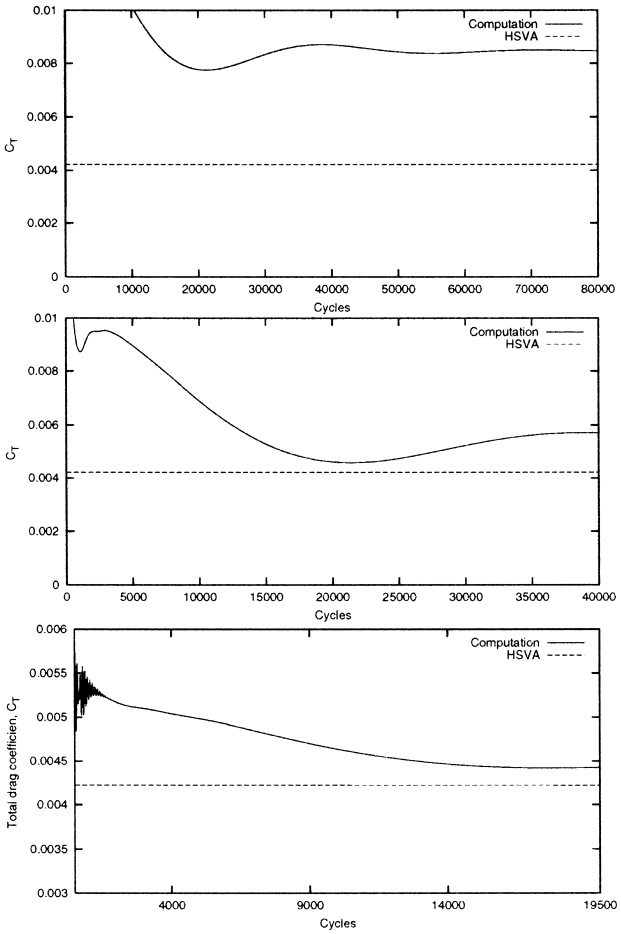

Figure 7. Convergence history of the total drag coefficient, C_T, the HTC model ($F_n = 0.25$ and $R_n = 1.255 \times 10^7$). Top: at the coarsest mesh ($36 \times 33 \times 12$). Middle: at the medium mesh ($71 \times 65 \times 23$). Bottom: at the finest mesh ($141 \times 129 \times 45$).

Table II. Grid convergence study of C_T ($\times 10^{-3}$) for the HTC model

Grids	C_T	E	Data
Level-3: $36 \times 33 \times 12$	8.473	N/A	4.222
Level-2: $71 \times 65 \times 23$	5.704	2.769	
Level-1: $141 \times 129 \times 45$	4.421	1.283	

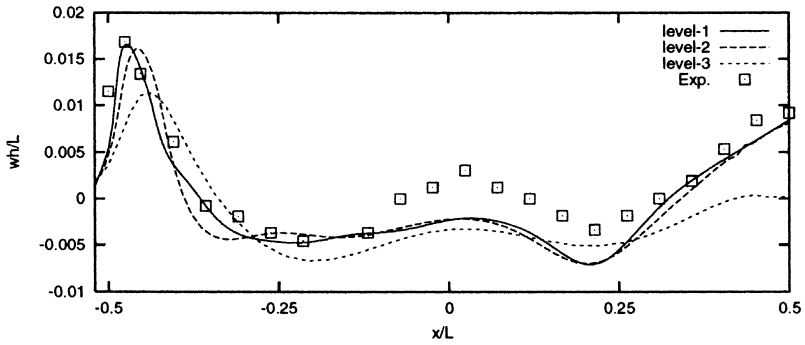

Figure 8. Grid refinement study and comparison of the surface-wave profiles with the experimental data, the HTC model ($F_n = 0.25$ and $R_n = 1.255 \times 10^7$). Level-1: $141 \times 129 \times 45$; level-2: $71 \times 65 \times 23$; level-3: $36 \times 33 \times 12$.

effect of the grid size within the boundary layer on the surface-wave profiles is weak but it is very important for prediction of a viscous resistance.

The grid convergence study for C_T from level-3 to level-1 is assessed, as given in Table II, where E is the relative error between successive grids. C_T at level-1 is closer to the data due to the smallest y^+ of 1.6.

Figure 9 illustrates the wave contours for these three levels, in which the difference between them is quite small in the region near the hull surface for level-1 and level-2. Nevertheless, it is apparent in the domain away from the hull surface, where the effects of the grid size on the free-surface waves are large for all the levels. This is similar to the study of Hino [12] for the case of a simple hull form, the Series 60 hull.

3.5. Wave profiles

A comparison of the calculated surface-wave profiles with the experiment is made in Figure 8. For level-1, the results agree very well with the experimental data except for those at the midship ($x/L = 0.0$), whereas those at level-2 can be reproduced well. The wave profiles after $x/L = 0.3$ are rather flat as compared with the bow wave peak due to the effect of the transom stern. This is a typical characteristic for this kind of ship form. It also implies that our dry-transom model works well. The reason for the discrepancy in the region at $x/L = 0.0$ is not clear. But the hump and hollow of the wave profiles within this range are well reproduced. An improvement is expected if the effects of the trim and sinkage are taken into account.

For the far-field waves at $y/L > 0.2$ off the hull surface, they are consistently underpredicted and lack detail [16]. Unfortunately, no experimental data are available for those at the $F_n = 0.25$. Thus, we consider the case of a higher $F_n = 0.28$ at the finest mesh due to the measurements available (the grid and the computational domain are the same as those mentioned above for $F_n = 0.25$). The results of the longitudinal wavecuts at $y/L = 0.1836$ and 0.2616 show very good agreement with the measured data in the bow region, as shown in Figure 10. Moreover, the transom stern waves are simulated well. Nevertheless, the difference

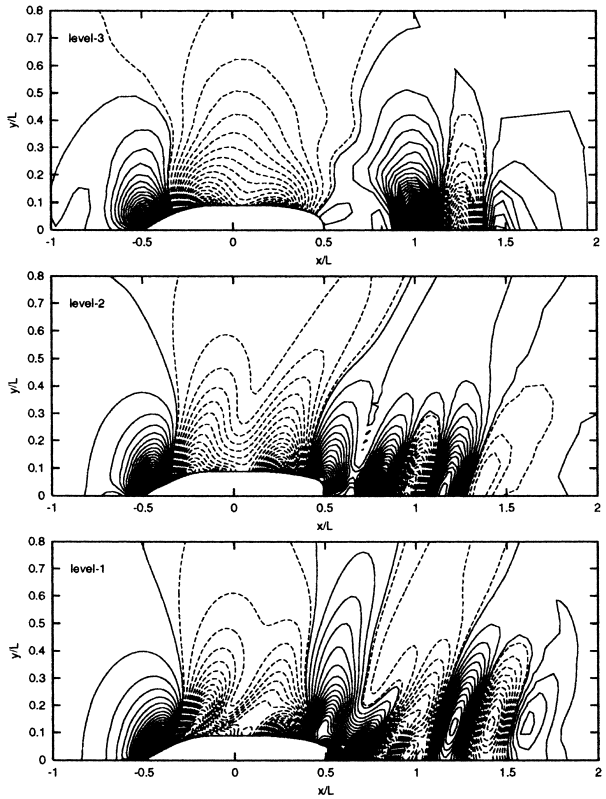

Figure 9. Wave contours at three grid levels, the HTC model ($F_n = 0.25$ and $R_n = 1.255 \times 10^7$). Level-1: $141 \times 129 \times 45$; level-2: $71 \times 65 \times 23$; level-3: $36 \times 33 \times 12$. Solid lines for crests; dashed lines for trough. Levels: 0.0003.

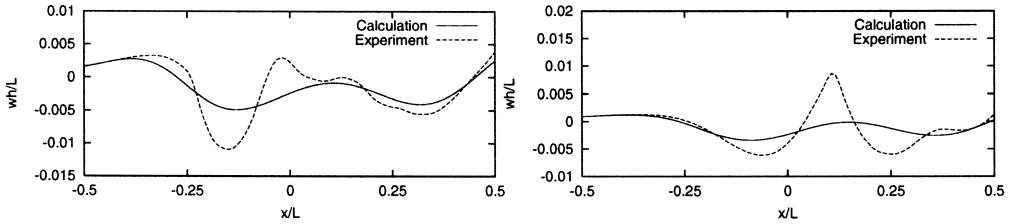

Figure 10. Comparison of the longitudinal wavecuts at the finest mesh with the experiment, the HTC model ($F_n = 0.28$ and $R_n = 1.443 \times 10^7$). Left: $y/L = 0.1836$. Right: $y/L = 0.2616$.

between the calculation and the experiment remains obvious at the midship. This requires further study.

3.6. Wave contours

The wave contours in Figures 9 and 11 show a typical characteristic of a container vessel with a transom stern. The systems of the divergent waves and the transverse waves are clearly

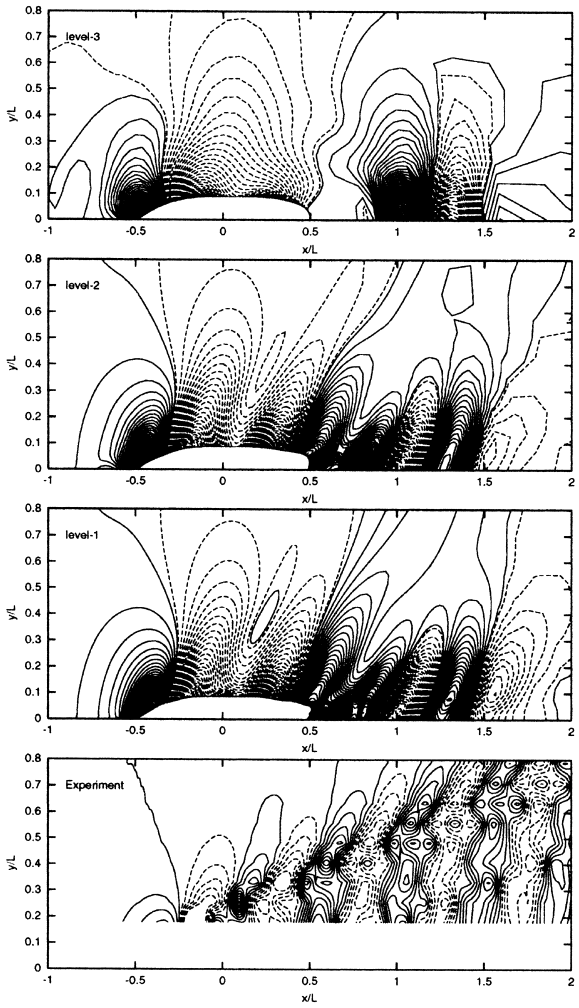

Figure 11. Comparison of the wave contours between the computations and the experimental data for three grid levels, the HTC model ($F_n = 0.28$ and $R_n = 1.443 \times 10^7$). Solid lines for crests; dashed lines for trough; levels: 0.0003. Level-1: $141 \times 129 \times 45$; level-2: $71 \times 65 \times 23$; level-3: $36 \times 33 \times 12$.

observed from these two figures and the former is dominant. The effect of the transom stern on the wave fields is also visible. It clearly diminishes the stern wave systems.

Figure 11 displays the wave contours for these levels at $F_n = 0.28$, including a comparison with the experimental data. For level-1 and level-2, the simulation captures well the near-field waves, especially for level-1, and the effects of the grid density on the waves in the domain close to the hull surface are also rather small even for a higher F_n. Nevertheless, there still remains a discrepancy between the computations and the measurements in the wake due to the damping.

3.7. Pressure distributions

Figure 12 presents the pressure contours on the hull surface at the finest mesh, where the pressure is made non-dimensional with the stagnation pressure $1/2\rho U^2$. It displays higher pressure at the bow than at the stern and low pressure at the midship (see Figure 12). This is common for this type of ship form.

3.8. Velocity fields

Figure 13 illustrates the velocity vectors (v, w) and the contours of the velocity (u) for level-1 at three cross-sections: close to the stern $(x/L = 0.90)$, at the propeller planer and in the near wake $(x/L = 1.01)$. The three components of velocities (u, v, w) are non-dimensionalized by the reference velocity U. At at $x/L = 0.9$, the thick boundary layer on the concave surface of the hull is well captured, and the thin boundary layer is obvious along the convex keel region (see Figure 13: top). At the propeller disk, the contours of the axial velocity show the round shape favourable to efficiency of the propeller, and a very weak vortex close to the upper corner of the propeller hub is also observed in Figure 13: middle. This vortex is not stronger than that in the wake at $x/L = 1.01$, as shown in Figure 13: bottom. In the wake, the contours of the velocity (u) display a rather slower recovery near the free surface.

The overall features in Figures 8–12 indicate the presence of the strong bow wave systems as well as the relatively weak stern wave systems. The former is clearly caused by higher pressure at the bow and the complicated interaction of the bulbous bow with the free surface. The latter is due to the effect of the transom stern. A shoulder wave system near the midship is also distinct. Therefore, the method successfully simulates the complex interaction of viscous flows with the free surface around the HTC model.

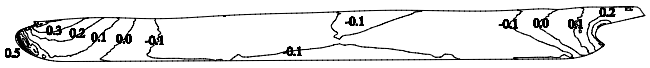

Figure 12. Pressure contours on the hull surface at the finest mesh, the HTC model ($F_n = 0.25$ and $R_n = 1.255 \times 10^7$).

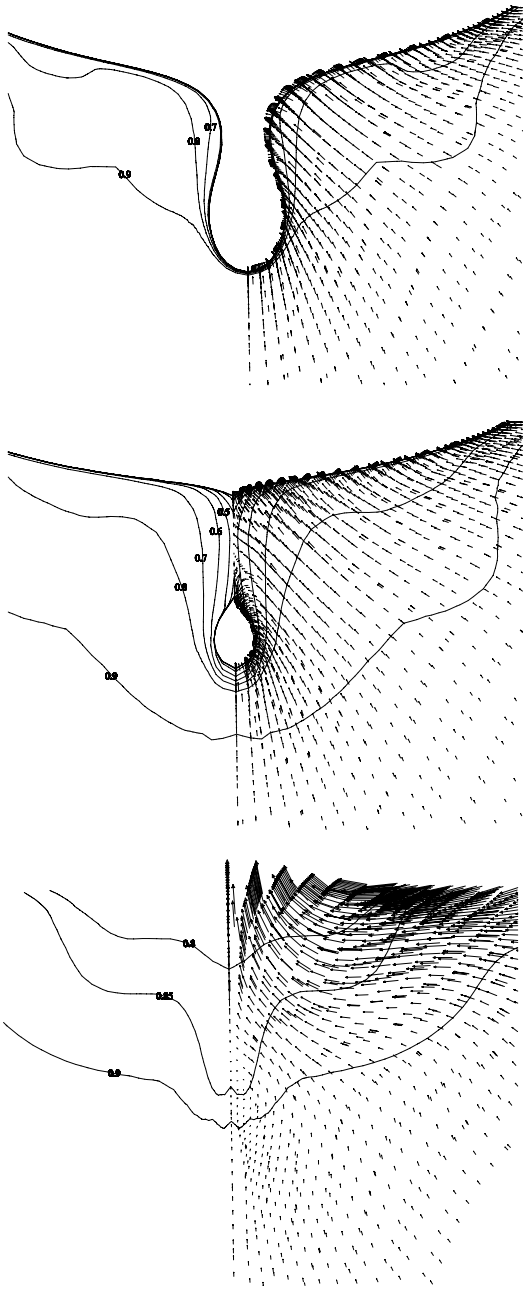

Figure 13. Velocity vectors (v, w) and the axial-velocity (u) contours at the finest mesh, the HTC model ($F_n = 0.25$ and $R_n = 1.255 \times 10^7$). Top: near the stern ($x/L = 0.9$). Middle: at the propeller disk. Bottom: in the wake ($x/L = 1.01$).

4. CONCLUSIONS

Based on the original FINFLO RANS solver, the method for simulation of viscous steady free-surface flows around realistic hull forms with a transom has been developed. The dry-transom model for the treatment of the flow off the transom has been proposed and it performs well. The calculated results are compared with the experimental data at two Froude numbers of 0.25 and 0.28. They agree well with the measured results available. Moreover, the method is capable of reproducing many features of the interaction of a viscous steady flow with the free surface. An overall degree of accuracy has been achieved by this method. It is expected that the present calculated results can provide information for analysis and design of the ship.

It should be noted that the damping of the far-field waves, especially in the wake, is strong due to the effects of viscous and/or the grid size. The adaptive grid could probably be improved for calculating results. Furthermore, we will consider the effects of the propeller and the appendages.

ACKNOWLEDGMENTS

The present work is sponsored by the Technology Development Centre (Tekes) in Finland. The first author would like to thank Professor Jerzy Matusiak for providing a chance to work in this project. Thanks also to Professor Timo Siikonen of the Laboratory of Applied Thermodynamics at Helsinki University of Technology, for his support and helpful technical discussion. Mr Tommi Mikkola and Esa Salminen gave us help. In addition, we thank the contribution of the Applied Hydrodynamics Group in VTT, and the help of Dr Antonio Sanchez-Caja, Dr Jaakko Pylkkanen and Mr Jussi Martio.

REFERENCES

1. Hino T. Numerical simulation of a viscous flow with a free surface around a ship model. *Journal of the Society of Naval Architects of Japan* 1987; **161**: 6–12.
2. Miyata H, Sato T, Baba N. Difference solution of a viscous flow with free surface about an advancing ship. *Journal of Computational Physics* 1987; **72**: 393–421.
3. Alessandrini B, Delhommeau G. Simulation of three-dimensional unsteady viscous free surface flow around a ship model. *International Journal for Numerical Methods in Fluids* 1994; **19**: 321–342.
4. Liu H, Ikehata M. Computation of free surface waves around an arbitrary body by a Navier–Stokes solver using the psuedocompressibility technique. *International Journal for Numerical Methods in Fluids* 1994; **19**: 395–413.
5. Kim JJ, Kim HT, Vam SH. RANS simulation of viscous flow and surface wave fields around ship models. In *3rd Osaka Colloquium on Advanced CFD Applications to Ship Flow and Hull Form Design*, Osaka, 1998; 105–123.
6. Wilson R, Paterson E, Stern F. Unsteady RANS CFD method for Naval combatant in waves. In *Proceedings of the 22nd Symposium on Naval Hydrodynamics*, Washington, DC, 1998; 1–17.
7. Tahara Y, Stern F. A large-domain approach for calculating ship boundary layers and wakes and wave fields for nonzero Froude number. *Journal of Computational Physics* 1996; **127**: 398–411.
8. Campana E, Mascio AD, Esposito PG, Lalli F. Viscous-inviscid coupling in free surface ship flows. *International Journal for Numerical Methods in Fluids* 1995; **21**: 699–722.
9. Tahara Y, Stern F, Rosen B. An interactive approach for calculating ship boundary layers and wakes for nonzero Froude number. *Journal of Computational Physics* 1992; **98**: 33–53.
10. Miyata H, Zhu M, Watanabe O. Numerical study on a viscous flow with free-surface waves about a ship in steady course by a finite-volume method. *Journal of Ship Research* 1992; **36**: 332–345.
11. Mori K, Hinatsu M. Viscous flow around Series 60 wave free-surface. In *Proceedings of CFD Workshop for Improvement of Hull Form Design*, Tokyo, Japan, vol. 2, 1994; 1–94.
12. Hino T. A study of grid dependence in Navier–Stokes Solution for free surface flows around a ship hull. *Journal of the Society of Naval Architects of Japan* 1994; **176**: 11–18.

13. Alessandrini B, Delhommeau G. A fully coupled Navier–Stokes solver for calculation of turbulent incompressible free surface flow past a ship hull. *International Journal Numerical Methods in Fluids* 1999; **29**: 125–142.
14. Saisto L, Sundell T. Computation of the viscous flow around the HSVA tanker. Report, Ship Laboratory, Helsinki University of Technology, Finland, 1996.
15. Miyata H. Time-marching CFD simulation for moving boundary problem. In *21th Symposium on Naval Hydrodynamics*, Trondheim, Norway, 1996.
16. ITTC. Report of the resistance and flow committee. In *22nd International Towing Tank Conference*, Seoul, Korea and Shanghai, China, vol. 1, 1999; 173–205.
17. Cowles G, Martinelli L. A viscous multiblock flow solver for free-surface calculations on complex geometries. In *Proceedings of the 22nd Symposium on Naval Hydrodynamics*, Washington, DC, 1998.
18. Muscari R, Broglio R, Di Mascio A. Comparison of three turbulence models for the study of the wake past a ship hull. In *Proceedings of the JAKOM'99*, Fukuuku, Japan, 1999.
19. Hino T. Navier–Stokes computations of ship flows on unstructured grid. In *Proceedings of the 22nd Symposium on Naval Hydrodynamics*, Washington, DC, 1998; 116–127.
20. Van SH, Kim WJ, Yim GT, Kim DH, Lee CJ. Experimental investigation of the flow characteristics around practical hull forms. In *Third Osaka Colloquium on advanced CFD Applications to Ship Flow and Hull Form Design*, Osaka, 1998; 215–227.
21. Haussling HJ, Miller RW, Coleman R. Computation of high speed turbulent flow about a ship model with a transom stern. ASME FED SM97, 1997.
22. Azcueta R, Muzaferija S, Peric M. Computation of water and air flow around ships. In *Proceedings of Euromech 374*, Poitiers, 1998.
23. Schumann C. Computing free surface ship flows with a volume-of-fluid method. *Proc. 7th PRADS 98 Conference*. Elsevier: Amsterdam, 1998.
24. Osher S, Sethian J A. Fronts propagating with curvature dependent speed: algorithms based on Hamilton–Jacobian formulas. *Journal of Computational Physics* 1998; **79**: 1–10.
25. Kawamura T, Miyata A. Simulation of non-linear ship flows by density-function method. *Journal of the Society of Naval Architects of Japan* 1995; **78**: 1–8.
26. Jeong JH, Yang DY. Finite element analysis of transient fluid flow with free surface using VOF (volume-of-fluid) method and adaptive grid. *International Journal for Numerical Methods in Fluids* 1998; **26**: 1127–1154.
27. Hamn-Ching C, Chen M. Chimera RANS simulation of a berthing DDG-52 ship in translations and rotational motions. *International Journal of Offshore and Polar Engineering* 1998; **8**: 182–191.
28. Siikonen T. *FINFLO User Guide*, *Version 2.2*. Laboratory of Applied Thermodynamics, Helsinki University of Technology: Finland, 1996.
29. Chorin AJ. A numerical method for solving incompressible viscous flow problems. *Journal of Computational Physics* 1967; **2**: 12–26.
30. Piippo H, Matusiak J, Sundell T. Computation of steady flow of Series 60 ship model. Report, Ship Laboratory, Helsinki University of Technology, Finland, 1998.
31. Rahman M, Rautaheimo P, Siikonen T. Numerical study of turbulent heat transfer from confined impinging jets using a pseudo-compressibility. Report No. 99, Laboratory of Applied Thermodynamics, Helsinki University of Technology, Finland, 1997.
32. Roe PL. Approximate Riemann solvers, parameter vectors, and difference schemes. *Journal of Computational Physics* 1981; **43**: 337–372.
33. Lombard CK, Bardina J, Venkatapthy E, Oliger J. Multi-dimensional formulation of CSCM—an upwind flux difference eigenvector split method for the compressible Navier–Stokes. In *6th AIAA Computational Fluid Dynamics Conference*, Danvers, MA, July, AIAA Paper 83-1895-CP, 1983; 649–664.
34. Jameson A, Yoon S. Multigrid solution of the Euler equations using implicit schemes. *AIAA Journal* 1986; **24**: 1–11.
35. Miettinen A, Siikonen T. An application of the multigrid technique to solve the pressure correction equation of incompressible flow. Report, Laboratory of Applied Thermodynamics, Helsinki University of Technology, Finland, 1997.
36. Baldwin B, Lomax H. Thin layer approximation and algebraic model for separated turbulent flows. In AIAA Paper 78-257, 1978.
37. Sundell T. Computation of the free surface flow around a ship model using the NS solver FINFLO. Report VALB279, VTT Manufacturing Technology/VAL3, Espoo, Finland.
38. Li T. Numerical simulation of viscous steady flow with free surface around two types of modern realistic hull forms: Hamburg Test Case and Tanker. Report M-247, Ship Laboratory, Helsinki University of Technology, Finland, 2000.

39. Li T. Benchmark test cases for viscous free-surface flows around modern surface ships: the HTC model, the KCS model, the DTMB 5415 model and the tanker model. Report, Ship Laboratory, Helsinki University of Technology, Finland, 2001.
40. Lehtimäki R. Grid deformation tools for simulation of free surface flows. In *6th International Conference on Numerical Field Simulation*, London, UK, 6–9 July 1998, 1998; 599–608.
41. Farmer J, Martinelli L, Jameson A, Cowles G. Fully non-linear CFD techniques for ship performance analysis and design. AIAA Paper 95-1690, AIAA 12th Computational Fluid Dynamics Conference, San Diego, CA, 1995.
42. Volker B, Kuo-Yih C, Gerd L, Jochen L. Experimental validation data of free-surface flows for cargo vessels. In *Proceedings of CFD Workshop*, Tokyo, Japan, 1994.

